Theoretical and Applied Fracture Mechanics 125 (2023) 103791

Contents lists available at ScienceDirect

Theoretical and Applied Fracture Mechanics

journal homepage: www.elsevier.com/locate/tafmec

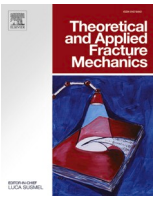

Mixed-mode dynamic fracture parameters for soda-lime glass

S. Dondeti, H.V. Tippur *

Department of Mechanical Engineering, Auburn University, AL 36849, United States

ARTICLE INFO

Keywords:
Soda-lime glass
Mixed-mode dynamic fracture
Optical measurements
Digital Gradient Sensing
Fracture envelope

ABSTRACT

Dynamic mixed-mode fracture of soda-lime glass (SLG) was experimentally investigated using a full-field optical method - Digital Gradient Sensing (DGS) - in conjunction with ultrahigh-speed photography. Single edge-notched specimens were subjected to reverse impact loading using a modified Hopkinson pressure bar. The specimens were eccentrically loaded at different offset distances relative to the initial notch to achieve a wide range of mode-mixities, from mode-I to nearly mode-II condition, at initiation. Two time-resolved orthogonal angular deflection fields of light rays proportional to the respective full-field stress gradients were optically measured during experiments on different geometries. Mode-I and -II stress intensity factor histories spanning pre- and post-initiation behaviors were evaluated via over-deterministic least-squares error minimization of optically measured full-field data. By considering the critical stress intensity factors at different crack initiation modes, a fracture envelope for SLG encompassing various mode-mixities was developed for the first time for SLG and compared with predictions from prevailing approaches. An empirical fit of data seems to capture the overall trend whereas the prevailing methods do not. Measured crack kink angles are compared with the popular MTS and SED fracture criteria; both predict the kink angles reasonably well. Unlike brittle polymers, the critical effective stress intensity factors for SLG are independent of mode-mixity over a large range of values but show a decreasing trend as mode-II conditions become dominant and an extrapolated critical mode-II stress intensity factor of 0.37 MPa$\sqrt{m}$, approx. one-half of its mode-I counterpart, is seen.

1. Introduction

Structures often fail in service due to combined tensile and shear loads resulting in mixed-mode fracture. Therefore, understanding the structural integrity under these conditions is critical. Here, the fracture characteristics of a rather challenging material system such as soda-lime glass, a widely used highly brittle structural material, is investigated under in-plane mixed-mode loading conditions by performing direct full-field optical measurements during stress wave loading events. It should be noted that previous investigations on this topic are generally limited to brittle polymers [1–11] and comparable works on glasses are not yet reported. For example, Mason et al. [1] studied dynamic mixed-mode, *K*-dominant, crack tip fields in PMMA using the coherent gradient sensing (CGS) method. The ability of that method to quantify dynamic mixed-mode crack tip deformations accurately was tested in their work. Guo et al. [2] studied dynamic mixed-mode fracture in three-point bend specimens using moiré interferometry technique along with ultrahigh-speed photography. The energy release rates and stress intensity factors were obtained via finite element analysis based on experimentally measured loads and crack propagation histories as inputs. Kirugulige and Tippur [3] studied mixed-mode dynamic fracture of functionally graded materials (FGM). They tested glass-filled epoxy sheets using reflection-mode CGS and high-speed photography to map instantaneous crack tip deformations. They noticed that when the crack was on the compliant side of the sample, it kinked significantly less when compared to when it was on the stiffer side. Kirugulige and Tippur [5] also measured mixed-mode fracture parameters in syntactic structural foams experiencing stress wave loading. They were among the first to use digital image correlation along with high-speed photography in that work and concluded that the mixed-mode crack growth generally occurred under dominant mode-I conditions. Jain and Tippur [6] investigated dynamic fracture in PMMA by extending reflection-mode digital gradient sensing (r-DGS) method for visualizing and quantifying fracture parameters. The stress intensity factor histories in the mixed-mode cases conformed well with the physical aspects both before and after crack initiation. Sundaram and Tippur [7] comparatively investigated dynamic fracture of two popular transparent polymers, PMMA and Polycarbonate, under mixed-mode loading conditions using transmission-mode DGS and developed fracture envelopes for each.

* Corresponding author.
E-mail address: tippuhv@auburn.edu (H.V. Tippur).

https://doi.org/10.1016/j.tafmec.2023.103791
Received 18 August 2022; Received in revised form 29 November 2022; Accepted 21 January 2023
Available online 26 January 2023

Nomenclature

e	eccentricity
W	width of the specimen
B	thickness of the specimen
a	initial notch length
υ	Poisson's ratio
L	distance between camera and specimen
Δ	distance between specimen and target plane
V	crack velocity
t	time instant
α(t)	orientation of crack at time instant t
K_I	mode-I stress intensity factor
K_{II}	mode-II stress intensity factor
K_{Icr}	mode-I critical stress intensity factor
K_{IIcr}	mode-II critical stress intensity factor
$(K_{eff})_{cr}$	critical effective stress intensity factor
ψ_{cr}	critical mode-mixity

Abbreviations

CGS	Coherent Gradient Sensing
DGS	Digital Gradient Sensing
DIC	Digital Image Correlation
FGM	Functionally Graded Material
Mfps	Million frames per second
MTS	Maximum Tensile Stress
PMMA	Poly(methylmethacrylate)
r-DGS	Reflection-mode Digital Gradient Sensing
SED	Strain Energy Density
SIF	Stress Intensity Factor
SLG	Soda-lime Glass
XFEM	Extended Finite Element Method

Mixed-mode dynamic fracture investigations in geomaterials - sandstone and granite - were carried out by Braunagel and Griffith [8]. They tested notched semi-circular specimens using a split Hopkinson pressure bar; to obtain various mixed-mode configurations, orientation of notch relative to loading direction was altered. Digital image correlation along with high-speed photography was employed to evaluate mode-I and mode-II stress intensity factors. Their results showed a decrease in energy release rate with increasing mode-mixity for Berea Sandstone. They also observed that mixed-mode propagation to be energetically favorable than pure opening mode propagation in sandstone, while the opposite to be true for granite. Snow et al. [9] investigated mixed-mode fracture of bovine cortical bone subjected to impact loadings. Aliha et al. [12] studied fracture toughness of Harsin marble under mixed-mode conditions ranging from pure mode-I to pure mode-III using edge-notched disc bend specimens. Their results indicated that the fracture toughness decreased with increase in mode-mixity.

Several numerical studies [4,13–18] on dynamic mixed-mode fracture mechanics have also been reported. Kirugulige and Tippur [4] numerically studied mixed-mode crack growth behavior in a compositionally graded glass-filled epoxy under dynamic conditions. A cohesive element methodology based on bilinear traction separation law was used to simulate mixed-mode dynamic crack growth. They captured the experimental characteristics of mixed-mode dynamic crack growth via finite element simulations. Asareh et al. [13] used a modified extended finite element method (XFEM) to study dynamic mixed-mode fracture. A non-nodal XFEM was developed within an explicit time integration scheme for modeling discontinuities in planar bodies and mimic mixed-mode crack propagation paths in three-point bending experiments. The dynamic mixed-mode fracture has also been studied using peridynamics for two-dimensional elastic cracked solids in Ref. [14]; three types of mixed-mode crack problems were investigated and dynamic stress intensity factors were evaluated. Cheng et al. [15] investigated dynamic fracture in functionally graded materials using peridynamics. The mixed-mode loading was enforced by applying eccentric impact load relative to the pre-crack, and their results agreed well with the experiments.

The primary goal of the current study is to investigate the mixed-mode dynamic fracture behavior of SLG, a very widely used engineering material. A secondary goal is to demonstrate the vision-based full-field optical method - DGS - for direct fracture parameter assessment in SLG at crack initiation, as it is the only technique to date sensitive enough to visualize and quantify mechanical fields near stationary and growing cracks in SLG [19,20]. To obtain mixed-mode fracture envelope for soda-lime glass, DGS method is used along with over-deterministic least-squares error minimization to evaluate fracture parameters at crack initiation. Also, a simple single-point reverse impact geometry capable of generating a wide range mode-mixities is proposed by quantifying mode-I and -II stress intensity factor histories during fracture events in different specimen loading configurations. Both fracture toughness and mode-mixity at crack initiation are extracted for SLG and the fracture characteristic relating the two is established for the first time. A fracture envelope is also established and comparatively examined relative to the Maximum Tensile Stress (MTS) criterion, Strain Energy Density (SED) criterion and an empirical relationship suggested in the geomaterials literature. In the following, experimental details including the specimen geometry and loading configuration, details regarding the optical method, the opto-mechanical setup are presented first. It is followed by a presentation of results on optical measurements and fracture parameters. Next, the results for SLG are discussed by considering comparisons relative to popular mixed-mode fracture theories before summarizing the contributions of the work.

2. Experimental details

2.1. Specimen geometry

Multiple rectangular SLG specimens of 50 mm × 100 mm dimension were extracted from a large 5.7 mm thick sheet, shown schematically in Fig. 1. Subsequently, a 12 mm long notch was cut into each specimen using a 150 μm thick diamond circular saw. While notching the specimen, natural microcracks are invariably generated around the tip. Hence, the results here are expected to correspond to the one due to a natural crack. To generate various mode-mixities at crack initiation, different offset (or eccentricity, e) distances between the loading and notch axes were employed while maintaining a constant notch length in all geometries.

Six geometric variants producing pure mode-I to dominant mode-II fracture at crack initiation were considered. Specifically, the specimens had eccentricities of $e = 0, 6, 12, 18, 24, 30$ mm with relative to the loading axis and a constant notch length of 12 mm. (A few details regarding the specimen geometry conception via elasto-dynamic finite element simulations are provided in the Appendix for completeness.) Some relevant mechanical and physical properties of soda-lime glass are listed in Table 1.

2.2. Optical method

In this work, a vision-based full-field optical method – Digital Gradient Sensing or DGS - was used to study dynamic fracture in SLG under mixed-mode loading conditions. A schematic representation of the setup used for DGS is shown in Fig. 2 to briefly explain its working principle. This technique utilizes 2D DIC to quantify pseudo speckle shifts that are proportional to two orthogonal in-plane stress gradients

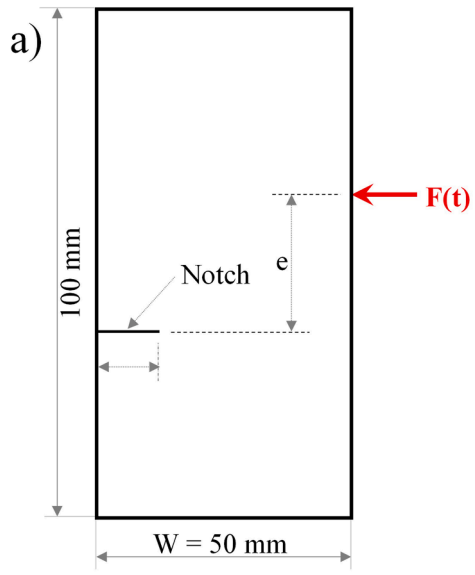

b)

Variants	Eccentricity, e, mm	Eccentricity ratio, e/W
1	0	0
2	6	0.12
3	12	0.24
4	18	0.36
5	24	0.48
6	30	0.60

Fig. 1. Specimen geometry details (a), different configuration with corresponding eccentricity values (b). (Plate thickness = 5.7 mm; initial notch length, a = 12 mm).

Table 1
Soda-lime glass properties [21].

Property	Value
Density, ρ	2500 kg/m^3
Longitudinal wave speed, C_L	5700 m/s
Shear wave speed, C_S	3400 m/s
Rayleigh wave speed, C_R	3100 m/s
Elastic modulus, E	70 GPa
Poisson's ratio, υ	0.22
Tensile strength, σ_t	41–180 MPa
Compressive strength, σ_c	330 MPa
Elasto-optic constant, C_σ	-0.027×10^{-10} m^2/N

when observed through planar specimens. A random speckle decoration on a planar surface called the 'target' is photographed through the region-of-interest in the specimen, see Fig. 2. The speckle pattern on the target is photographed first through the undeformed specimen to obtain a reference image. By correlating the speckle images in the reference and deformed states, pseudo local shifts in speckle clusters, δ_x and δ_y, caused by the so-called elasto-optic effect are quantified. Knowing the distance Δ between the specimen and the target planes from the experimental setup, the angular deflections of the light rays ϕ_x and ϕ_y in two orthogonal planes, x-z and y-z planes, respectively, can be subsequently evaluated. The angular sweeps ϕ_x and ϕ_y are shown to be proportional to the gradients of the in-plane normal stresses as [22],

$$\phi_{x;y} = \pm C_\sigma B \frac{\partial(\sigma_x + \sigma_y)}{\partial x; y} \tag{1}$$

where C_σ is the elasto-optic constant of the material, B is its initial thickness, $(\sigma_x + \sigma_y)$ is the first stress invariant of stress under plane stress condition, and σ_x and σ_y denote the thickness-wise averages of Cauchy's normal stress components. Note that the measurements correspond to the target plane coordinates but can be mapped to the specimen plane by a mapping function, $(x; y) \times (L + \Delta) = (x_o; y_o) \times L$ where L and Δ represent distances between the camera and the specimen and specimen and the target planes, respectively. In addition, the value of Δ can be tuned to change the measurement sensitivity as needed based on the material being studied.

2.3. Opto-Mechanical experimental setup

Fig. 3 shows the opto-mechanical setup used in the experiments. To study mixed-mode dynamic fracture, a long-bar impactor was used in conjunction with the DGS technique and ultrahigh-speed photography. The long-bar was 1800 mm long and 25.4 mm in diameter C-300 maraging steel rod. It had a semi cylindrical tip to load the SLG specimen placed on a soft putty strip along the top and bottom edges, as shown in inset of Fig. 3. This created geometric symmetry in terms of acoustic impedance while providing approx. free boundary conditions along those edges. The stress waves were generated by launching a 305 mm long, 25.4 mm diameter steel cylindrical striker at a velocity of ~ 5.3 m/s to impact the long-bar. The striker velocity was kept relatively low in order to achieve inertially driven crack initiation without crushing the material at the loading point and emanate cracks there instead of the one at the precut notch tip. The striker/long-bar contact triggered the camera to record speckles on the target plane through the specimen. A Kirana (model #05 M) ultrahigh speed camera (from Specialized Imaging, Inc.) was used to capture speckle images at 1 Mfps. The distance between the specimen and the camera was 3.86 m whereas the target and the specimen was 1 m. The camera was fitted with a Nikkor 400 mm f/2.8 macro lens with a 2X tele-converter and adjustable bellows. An F$^{\#}$16 aperture setting was used for a good depth of focus and sensor exposure. To obtain speckle pattern on the target, black and white speckles were spray painted alternatively on a planar polymer sheet until a homogenous but random pattern was attained. Relatively fine pattern was generated to be able to capture angular deflections of light rays due to sub-micron scale deformations expected around the crack-tip. A magnification factor of 118 μm/pixel on the target plane (or 94 μm/pixel on the specimen plane) was used.

3. Results

3.1. Stress Gradient histories

Fig. 4 shows a pair of recorded speckle images at time instants t = -37 μs and 0, respectively; the former is in the reference/undeformed state and the latter corresponds to crack initiation. The specimen edges, initial notch and crack tip location are highlighted in Fig. 4. The speckle fields themselves are not very informative except for some smearing near locations of significant deformations near the loading point and the crack tip upon careful examination. Upon correlating the speckle fields from the reference and deformed states, however, the mechanical fields become vividly evident. The angular deflections of light rays ϕ_x and ϕ_y in the two orthogonal directions (with respect to the initial notch) at select time instants for select geometries are shown in Fig. 5 and Fig. 6 as contour maps for showing morphological differences in the resulting mechanical fields obtained from different specimen geometries. Animations of evolving angular deflection contours of ϕ_x and ϕ_y for eccentricity ratio of e/W = 0.48 configuration are included in

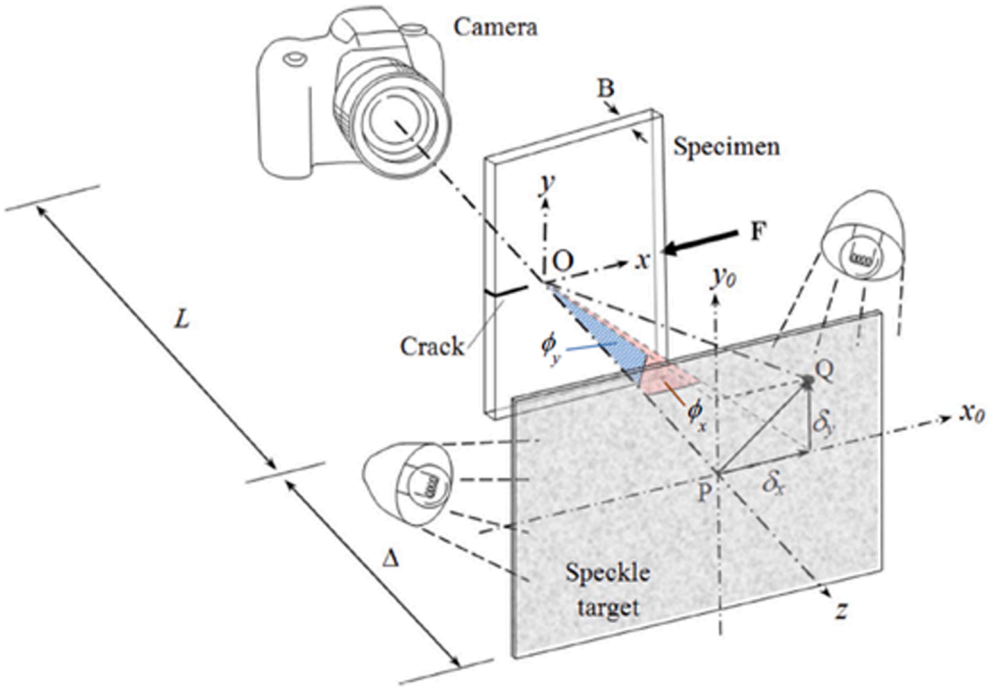

Fig. 2. The schematic representation of Digital Gradient sensing (DGS) technique to determine planar stress gradients.

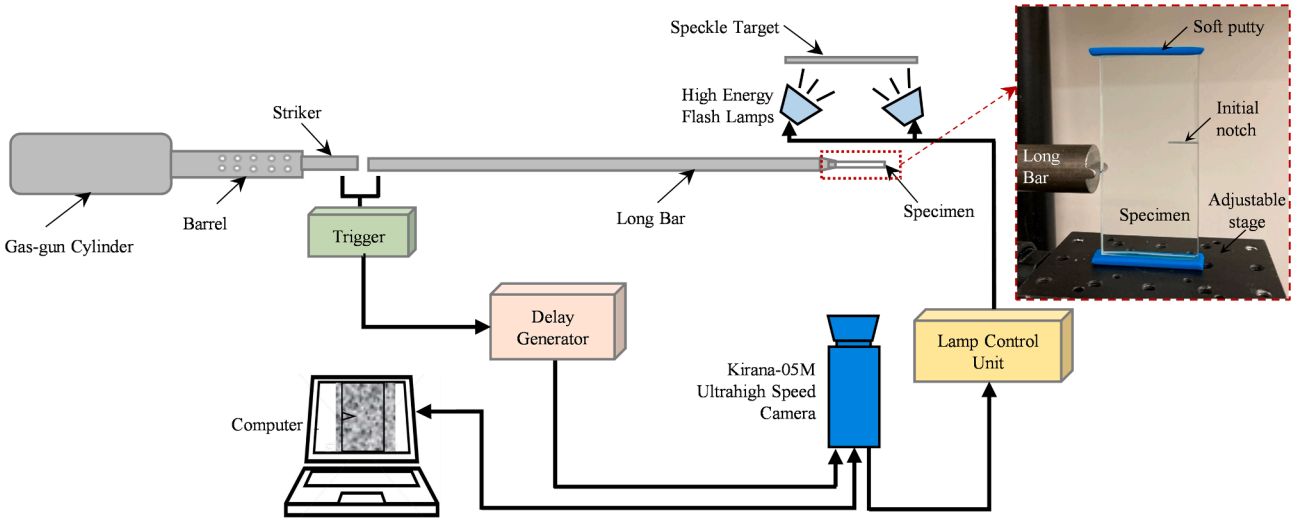

Fig. 3. The schematic of experimental setup for transmission DGS measurements.

Supplementary Materials. For visualization purposes, the animations include early stages of loading where the mechanical fields/contour maps are evident at the impact location followed by the ones at the crack tip until mixed-mode crack initiation and subsequent crack propagation. The optical analysis included segmenting the recorded speckle image in the reference and deformed states into 30 × 30 pixels size subsets. The location of a subset in the deformed state relative to its reference state was determined by performing a gray scale correlation using ARAMIS® (GOM mbH, Braunschweig, Germany) software. During analysis, a subset overlap of 5 pixels was used to balance computational effort and experimental noise. Once the location of a subset in the deformed state was identified, the local speckle shifts were quantified at the center of each subset. This resulted in two data arrays of 146 × 132 size corresponding to speckle shifts in the horizontal and vertical directions, respectively, at each time instant. They were subsequently used to compute angles ϕ_x and ϕ_y by dividing the psuedo speckle shifts by the distance between the specimen and target planes. Note that at each time instant the data in the whole field was available as rectangular arrays and were used to plot contour maps for visualization purposes. The specimen edges along with the initial notch are highlighted in Fig. 5. Here, the timestamps are with respect to the instant when the crack initiated ($t = 0$) at the initial tip. The first column in Fig. 5 represents ϕ_x contours before crack initiation at a time instant, t = -3 μs, for three select eccentricity ratios. The second column shows contour maps at crack initiation or at $t = 0$ and the last column represents contour plots during crack propagation. The first row represents pure mode-I loading

variant, where ϕ_x contours are symmetric relative to the dominant mode-I crack path. The second row represents ϕ_x contours with an eccentricity ratio of $e/W = 0.24$ and the contours are asymmetric about the initial notch. The ϕ_x contours in the last row represents mode-II dominant loading case with an eccentricity ratio of $e/W = 0.48$. In this case, due to the higher mode-mixity, the shape of ϕ_x contours appear to have rotated significantly relative to the one in the first row. In Fig. 6, ϕ_y contours at select time instants for the corresponding three different eccentricity ratios are plotted. Again, the first row depicts ϕ_y contours of pure mode-I condition; hence the contour shapes are anti-symmetric with respect to the initial notch. With an increase in the eccentricity ratio to $e/W = 0.24$, the ϕ_y contours become asymmetric as the crack tip in this case is subjected to mixed-mode loading. At a higher eccentricity ratio of $e/W = 0.48$, the crack tip experiences a dominant mode-II loading, and hence the ϕ_y contours appear to have rotated significantly relative to the mode-I counterparts. It is noteworthy that from these two sets of angular deflection contours, locating the crack tip is relatively straight forward due to the singular nature of the mechanical fields [19]. That is, the contours representing each of the measured fields have a lobed structure that converges to the crack tip, marked in Fig. 5 and Fig. 6 by a solid white dot/circle, making it relatively easy to locate it at each time instant. Any uncertainty can be further resolved by considering contours of resultant angular deflection, $\sqrt{\phi_x^2 + \phi_y^2}$, which produce closed contours encircling the instantaneous crack tip and easy to identify [23].

3.2. Stress intensity factor histories

The stress gradient fields at each instant of time were analyzed by using a least-squares minimization of measured data along with the corresponding angular deflection fields of light rays [24]. The analysis was performed in the local crack tip coordinates (x', y') where x' coincides with the crack growth direction at that instant and oriented at an angle α(t) relative to the global (x, y) coordinates. The angular deflection field $\phi_{x'}$ was analyzed in this work using the coordinate transformation equation,

$$\phi_{x'}(t) = \phi_x(t)\cos\alpha(t) + \phi_y(t)\sin\alpha(t) \tag{2}$$

The angular deflection contours ϕ_x and $\phi_{x'}$ in both global and local coordinates 8 μs after crack initiation is shown in Fig. 7. As to be expected, the ϕ_x contours are asymmetric relative to the crack tip location whereas the $\phi_{x'}$ contours are more symmetric with respect to the instantaneous crack tip propagation direction, x', suggesting crack growth under locally dominant mode-I conditions. The measured data was fitted using the asymptotic expression,

$$\phi_{x'} = C_\sigma B\left[\begin{array}{c} -\frac{1}{2}r_l^{-\frac{3}{2}}\left\{f(V)A_1(t)\cos\left(\frac{3\theta_l}{2}\right) + g(V)D_1(t)\sin\left(-\frac{3\theta_l}{2}\right)\right\} \\ +\sum_{N=2}^{\infty}\left\{A_N(t)\left(\frac{N}{2}-1\right)r_l^{\left(\frac{N}{2}-2\right)}\cos\left(\left(\frac{N}{2}-2\right)\theta_l\right) + D_N(t)\left(\frac{N}{2}-1\right)r_l^{\left(\frac{N}{2}-2\right)}\sin\left(\left(\frac{N}{2}-2\right)\theta_l\right)\right\} \end{array}\right] \tag{3}$$

in the local coordinates where x' and y' denote the standard crack tip coordinates aligned with the instantaneous crack orientation. Here C_σ is the elasto-optical constant for SLG (see, Table 1), and B is the specimen thickness. The functions f and g in Eq. (3) are functions of crack velocity V, and (r_l, θ_l) denote the local crack tip polar coordinates given by, $r_l = \sqrt{(x')^2 + \alpha_L^2(y')^2}$ and $\theta_l = \tan^{-1}\left(\frac{\alpha_L y'}{x'}\right)$. Explicitely they are, $f(V) = \left(\frac{1+\nu}{1-\nu}\right)\frac{(1+\alpha_S^2)(1-\alpha_S^2)}{4\alpha_S\alpha_L - (1+\alpha_S^2)^2}$ and $g(V) = \left(\frac{1+\nu}{1-\nu}\right)\frac{2\alpha_S(1-\alpha_L^2)}{4\alpha_S\alpha_L - (1+\alpha_S^2)^2}$ where $\alpha_L = \sqrt{1 - \frac{\rho(1-\nu)}{2\mu}V^2}$, $\alpha_S = \sqrt{1 - \frac{\rho}{\mu}V^2}$ for plane stress, μ and ρ are shear modulus and mass density, respectively. The mode-I and -II stress intensity factors are related to $A_1(t)$ and $D_1(t)$ in Eq. (3) as $K_I(t) = \sqrt{\frac{\pi}{2}}A_1(t)$ and $K_{II}(t) = \sqrt{\frac{\pi}{2}}D_1(t)$. The optical data in the crack tip vicinity $0.35 \leqslant r/B \leqslant 1.35$ and $-150^\circ \leqslant \theta \leqslant 150^\circ$ was considered while extracting the two stress intensity factors. Also, the analysis included higher order terms up to $N = 4$ in the stress field and was guided by previous works [19,23,25] using DGS. In Eq. (3). It should also be noted that the first higher order term in Eq. (3) vanishes. Hence the measured stress gradient fields from DGS are insensitive to the so-called T-stress and is unavailable for analysis.

The SIF histories extracted for different mixed-mode variants from DGS data are shown in Fig. 8. Here again, time $t = 0$ corresponds to crack initiation at the initial tip. The mode-I SIFs, K_I, are shown with solid symbols and the mode-II SIFs, K_{II}, with open symbols, respectively. Fig. 8 (a) shows SIF histories for a selected set of experiments from all mixed-mode configurations studied. The mode-I SIF, K_I, of the specimen with a zero-eccentricity ratio (*e/W* ratio) increased steadily from nearly zero value to ~ 0.72 MPa$\sqrt{\text{m}}$ over ~ 15 μs period. The fracture toughness obtained under mode-I loading condition is similar to the values obtained from the previous studies [19,23]. After initiation, the mode-I SIF, K_I, is nearly constant for about 2 μs and increased again until the end of the observation window. The SIF histories are shown only for 5 μs after crack initiation since the crack tip fields start interacting with those in the loading region significantly after that. Meanwhile, the corresponding instantaneous mode-II SIF values, K_{II}, expectedly remained low. With post-initiation growth expected to occur under dominant mode-I conditions locally, one could view the mode-II SIF values to represent error estimates from the least-square error minimization method adopted here. Next, with an eccentricity ratio of $e/W = 0.12$, the K_I values increased steadily until initiation, similar to $e/W = 0$ case. However, the K_I values tracked below the latter case until initiation and the fracture toughness at initiation, K_{Icr}, was ~ 0.65 MPa$\sqrt{\text{m}}$ in this specimen. After initiation, the mode-I SIF dropped and continued to increase, similar to the trend observed in $e/W = 0$ case. The mode-II SIF, K_{II}, for $e/W = 0.12$ variant also increased steadily in *magnitude* and reached a value of ~ -0.31 MPa$\sqrt{\text{m}}$ at initiation.

Once the crack initiated, the negative mode-II SIF values flipped to positive values and transiently fluctuated for ~ 3 μs before reducing to ~ 0.09 MPa$\sqrt{\text{m}}$ at 5 μs. With a further increase in the eccentricity ratio, the mode-I SIF values decreased. The critical mode-I SIFs for e/W = 0.24, 0.36, 0.48 and 0.60 were ~ 0.50 MPa$\sqrt{\text{m}}$, 0.35 MPa$\sqrt{\text{m}}$, 0.17 MPa$\sqrt{\text{m}}$, and 0.07 MPa$\sqrt{\text{m}}$, respectively, and the post initiation mode-I SIF values also show similar trends observed in e/W = 0 and 0.12 cases. It is noteworthy that the magnitude of mode-II SIF increased until e/W = 0.48 case and decreased for e/W = 0.60 case. The corresponding

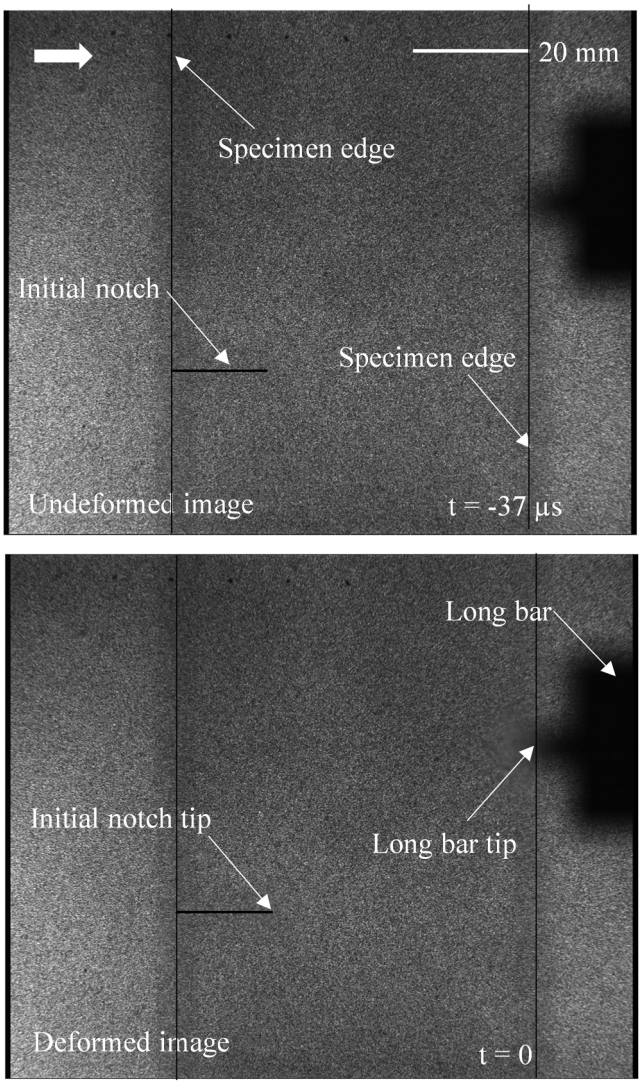

Fig. 4. Speckle images from in the undeformed (top) and deformed (bottom) states recorded by ultrahigh speed camera. (The heavy arrow represents crack growth direction towards the load.).

mode-II values were ~ -0.33 MPa$\sqrt{m}$, −0.48 MPa$\sqrt{m}$, −0.52 MPa$\sqrt{m}$, and −0.41 MPa$\sqrt{m}$. In the post initiation phase, the mode-II SIF values flipped to positive values and fluctuated for a few microseconds due to the transients before reducing to small values. In each case from e/W = 0 to 0.60, two to four experiments were conducted to ensure repeatability. Fig. 8(b) and (c) show SIF histories for multiple $e/W = 0.12$ and 0.36 cases; reasonably good repeatability and data trends are seen given the challenging brittle material system being investigated. The loading rates in each case was also estimated as time-rate of change ofK_{eff}, or$\dot{K}_{eff}$, using data just prior to crack initiation. The $\dot{K}_{eff}$ values were all in the GPa$\sqrt{m}$/s; specifically, they were ~ 113 GPa$\sqrt{m}$/s, 106 GPa$\sqrt{m}$/s, 78 GPa$\sqrt{m}$/s, 67 GPa$\sqrt{m}$/s, 56 GPa$\sqrt{m}$/s and 35 GPa$\sqrt{m}$/s for $e/W = 0$, 0.12, 0.24, 0.36, 0.48 and 0.6, respectively.

4. Discussion

Measurements described above were compiled into plots of critical effective SIF ($(K_{eff})_{cr} = \sqrt{K_{Icr}^2 + K_{IIcr}^2}$) and critical mode-mixity ($\psi_{cr} = \left|\tan^{-1}\left(\frac{K_{Icr}}{K_{IIcr}}\right)\right|$) at crack initiation in Fig. 9(a) and (b) as a function of e/W, the specimen dependent geometric parameter. The $(K_{eff})_{cr}$ values are nearly constant for e/W ratios up to 0.36 with a decreasing trend seen at higher values of e/W namely, 0.48 and 0.6. The ψ_{cr} values on the other hand show a monotonically increasing trend over the entire e/W range examined. Using these two plots and by eliminating the geometric parameter e/W, a mixed-mode fracture characteristic plot for SLG was generated for the first time and is shown in Fig. 9(c). It suggests that the critical fracture toughness evaluated as $(K_{eff})_{cr}$ of SLG is generally independent of mode-mixity at crack initiation until a mode-mixity of ~ 65°. Beyond that and up to a mixity of ~ 85° achieved in the current work, there is a visible drop in the $(K_{eff})_{cr}$ value to ~ 0.45 MPa$\sqrt{m}$ and an extrapolated value of ~ 0.37 MPa$\sqrt{m}$ at ψ_{cr} of 90° or the pure mode-II condition. This is somewhat counter to the mixed-mode fracture behaviors of ceramics such as alumina and zirconia [26] and soft stones reported in the literature. It is likely attributed to the amorphous nature of SLG. That said, there are reports in the literature where a drop in the strength of borosilicate glass and soda-lime glass with increasing shear in shear-compression tests [27,28] is observed. Furthermore, Johnston et. al [29] and Mirsayar et. al [30,31] have reported a reduction in the fracture toughness of Johnstone, Neyriz and Harsin marble rock materials at higher mode-mixities, suggesting consistency of the present observation with those reports.

A fracture envelope was also generated using the critical mode-I and mode-II SIF values, K_{Icr} andK_{IIcr}, obtained using the methodology detailed previously. The resulting plot is shown in Fig. 10 using solid symbols. The fracture envelope was compared with two popular mixed-mode crack propagation criteria for brittle materials. First, the Maximum Tangential Stress (MTS) criterion [32,33] was considered. As per the MTS criterion, crack should grow in a direction perpendicular to the maximum hoop stress,$\sigma_{\theta\theta}$, at the crack tip when the hoop stress reaches a critical value. It is governed by,

$$K_I \cos^3\frac{\theta_{cr}}{2} - \frac{3}{2}K_{II}\cos\frac{\theta_{cr}}{2}\sin\theta_{cr} = K_{Icr} \tag{4}$$

where θ_{cr} is the crack kink angle. Next, the Strain Energy Density (SED) criterion [33] was also used to compare it with the experimental results. As per the SED criterion, crack should propagate in a direction of minimum SED, $S(\theta)$ given by,

$$S(\theta) = \left(\frac{1}{\pi}\right)\left(g_{11}K_I^2 + 2g_{12}K_IK_{II} + g_{22}K_{II}^2\right) \tag{5}$$

$$\begin{Bmatrix} g_{11} \\ g_{12} \\ g_{22} \end{Bmatrix} = \left(\frac{1}{16\mu}\right)\begin{bmatrix} (1+\cos\theta_{cr})(\eta-\cos\theta_{cr}) \\ 2\cos\theta_{cr} - (\eta-1) \\ (\eta+1)(1-\cos\theta_{cr}) + (1+\cos\theta_{cr})(3\cos\theta_{cr}-1) \end{bmatrix}$$

μ = shear modulus, $\eta = \frac{3-\upsilon}{1+\upsilon}$ for plane stress, and propagate when minimum SED reaches a critical value $S_{cr}(\theta)$.

Evidently, both MTS and SED criteria are not very representative of the measured data at higher mode-mixities with the latter following the trend better than the former. It is also worth noting that an empirical curve of the type,

$$\left(\frac{K_{Icr}}{0.67}\right)^{2.55} + \left(\frac{K_{IIcr}}{0.57}\right)^{2.55} = 1 \tag{6}$$

has been shown to fit the soft stone (Johnstone) data better in Ref. [29]. The resulting empirical fit is also shown in Fig. 10. Again, the agreement between the fit and the data is not satisfactory particularly at higher mode-mixities. Accordingly, a different empirical fit of the type,

$$C_1K_{Icr}^2 + C_2K_{IIcr}^2 + C_3K_{Icr} + C_4K_{IIcr} + C_5 = 0 \tag{7}$$

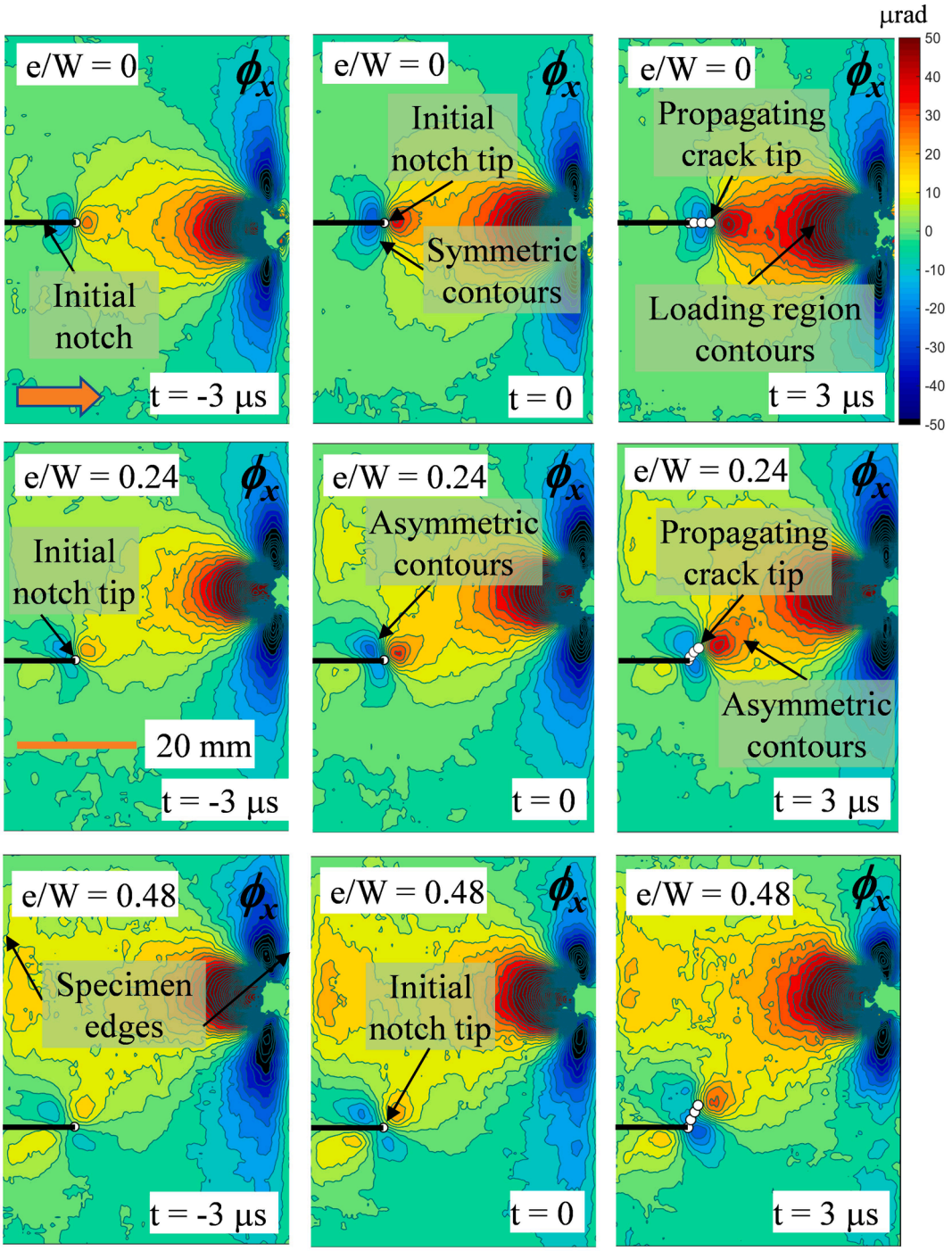

Fig. 5. Contours of angular deflection of light rays (contour increment = 5×10^{-6} rad) in *x-z* plane in soda lime glass plate at select time instants. The arrow head in the top left shows crack growth direction. (Time, $t = 0$ corresponds to crack initiation at initial notch tip.).

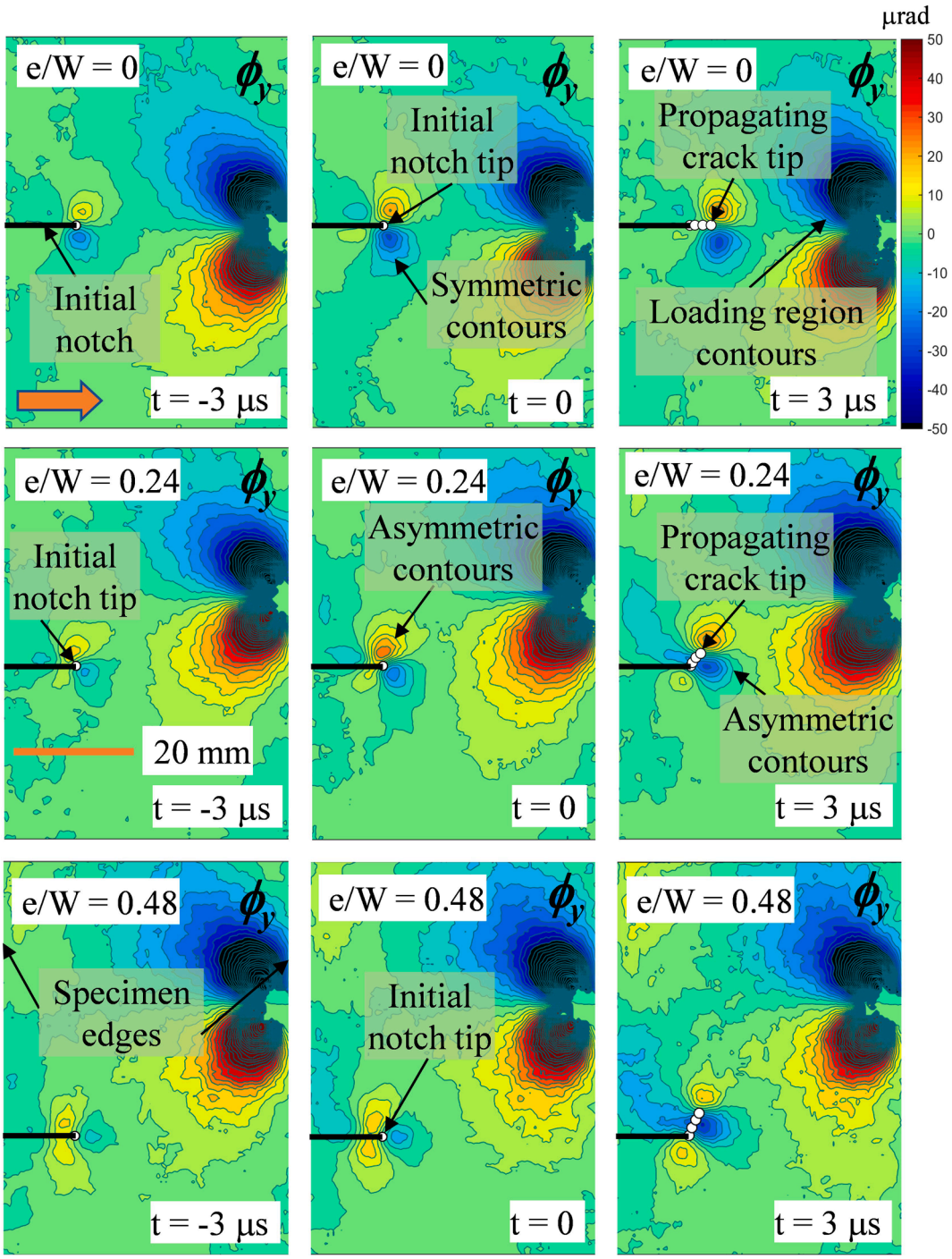

Fig. 6. Contours of angular deflection of light rays (contour increment = 5×10^{-6} rad) in *y-z* plane in soda lime glass plate at select time instants. The arrowhead in the top left shows crack growth direction. (Time, $t = 0$ corresponds to crack initiation at initial notch tip.).

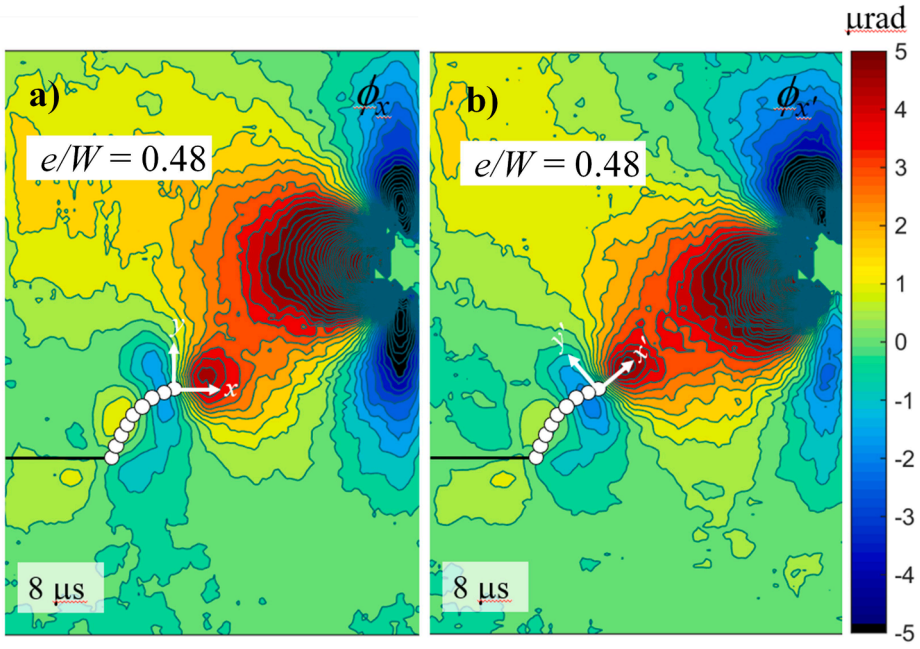

Fig. 7. Contours of angular deflections of light rays (contour increment = 5×10^{-6} rad) in (a) global coordinates (x-z plane) and (b) local coordinates (x'-z plane) at select time instant during kinked crack growth for $e/W = 0.48$ configuration. The white markers represent crack tip locations at the current and previous time instants.

where $C_1 - C_5$ are constants was considered. A fit with $C_1 = 2.21$, $C_2 = 1$, $C_3 = 0$, $C_4 = -1.36$ and $C_5 = 0.13$ represents the data trend well over the entire range. The corresponding critical values for pure mode-I and mode-II conditions are 0.71 and 0.37 MPa$\sqrt{m}$, respectively.

Next, the kink angles from failed specimens were also measured from fractured specimens and compared directly with the ones from MTS and SED criteria. Fig. 11 shows magnified views of fractured specimens with increasing eccentricity. For better visual clarity, only lower part of the fractured specimens is shown. The measured kink angle from mixed-mode experiments were 33°, 47°, 52°, 63° and 68° for eccentricity ratios, e/W, of 0.12, 0.24, 0.36, 0.48 and 0.60, respectively, with a ± 2° measurement accuracy. The kink angles from MTS criterion were evaluated using,

$$K_I\left[-\sin\frac{\theta_{cr}}{2}-\sin\frac{3\theta_{cr}}{2}\right]+K_{II}\left[-\cos\frac{\theta_{cr}}{2}-3\cos\frac{3\theta_{cr}}{2}\right]=0 \tag{8}$$

$$K_I\left[-\cos\frac{\theta_{cr}}{2}-3\cos\frac{3\theta_{cr}}{2}\right]+K_{II}\left[\sin\frac{\theta_{cr}}{2}+9\sin\frac{3\theta_{cr}}{2}\right]<0 \tag{9}$$

using measured critical SIFs at crack initiation (Fig. 10).

The results are compared with the ones measured from the fractured specimens in Table 2. The kink angles from the MTS criterion for eccentricity ratios of $e/W = 0$, 0.12, 0.24, 0.36, 0.48 and 0.60 was 11°, 39°, 51°, 59°, 65° and 68°, respectively, and are in reasonably good agreement but for the mode-I case which produced a small yet distinct kink while initiating from the notch tip. The SED criterion was also used for estimating crack kink angles by satisfying the below equations:

$$[2\cos\theta_{cr}-(\eta-1)]\sin\theta_{cr}K_I^2+2[2\cos2\theta_{cr}-(\eta-1)\cos\theta_{cr}]K_IK_{II}+[(\eta-1-6\cos\theta_{cr})\sin\theta_{cr}]K_{II}^2=0 \tag{10}$$

$$[2\cos(2\theta_{cr})-(\eta-1)\cos\theta_{cr}]K_I^2+2[(\eta-1)\sin\theta_{cr}-4\sin(2\theta_{cr})]K_IK_{II}+[(\eta-1)\cos\theta_{cr}-6\cos(2\theta_{cr})]K_{II}^2>0 \tag{11}$$

where η a function of Poisson's ratio (assumed to be = 2.28 for SLG and plane stress condition). The resulting kink angles are also tabulated in Table 2. The kink angles obtained from the SED criterion for eccentricity ratio of $e/W = 0$, 0.12, 0.24, 0.36, 0.48 and 0.60 was 9°, 33°, 44°, 56°, 67° and 72°, respectively, again in reasonable agreement with the measurements. Thus, both MTS and SED criteria show a reasonably good match with the kink angles of fractured specimens.

5. Conclusions

An optical investigation of mixed-mode dynamic fracture behavior of a challenging material namely soda-lime glass was undertaken. A simple reverse impact specimen geometry with a constant crack length but subjected to eccentric loading was employed to create mode-mixities from mode-I to nearly mode-II conditions at crack initiation. The impact loading was achieved using a long-bar loading apparatus and crack tip mechanical fields were mapped in real-time by employing the Digital Gradient Sensing (DGS) method along with ultrahigh-speed photography. The stress gradients in two mutually perpendicular in-

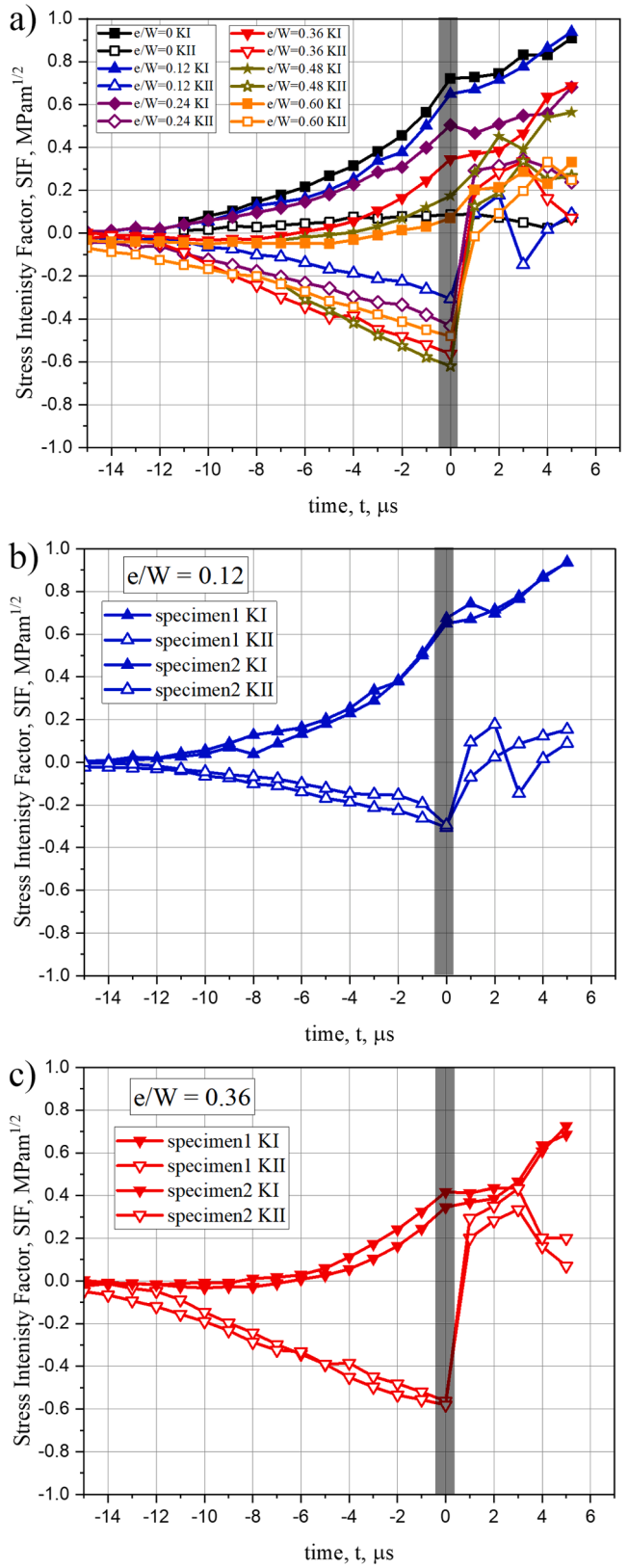

Fig. 8. Stress intensity factor histories (a) for selected experiments from all mixed-mode configurations, (b) repeatability experiments from eccentricity ratio, $e/W = 0.12$ case and (c) repeatability experiments from eccentricity ratio, $e/W = 0.36$ case of soda-lime glass specimens subjected to dynamic loading. (Time, $t = 0$ corresponds to crack initiation at initial notch tip.).

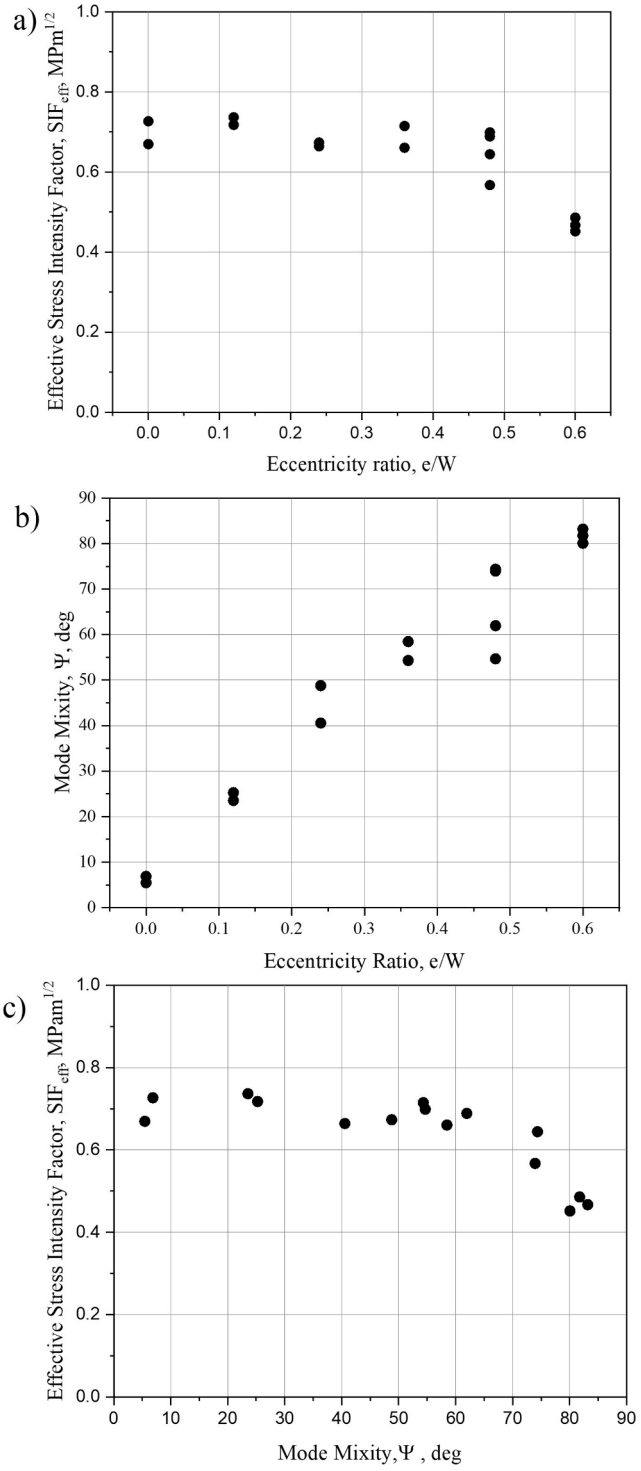

Fig. 9. Compilation of measured fracture parameters for SLG from different mixed-mode fracture experiments: (a) Dependence of effective critical stress intensity factor on eccentricity, (b) Dependence of mode-mixity on eccentricity and (c) Variation of effective critical stress intensity factors with mode-mixity.

plane direction were visualized and quantified by measuring angular deflections of light rays from the early stages of loading to crack initiation and subsequent crack propagation. From the time-resolved measurements, mode-I and mode-II SIF histories were extracted by performing over-deterministic least-squares minimization of optical data along with prevailing asymptotic description of the crack tip fields. A monotonic increase in mode-mixity at crack initiation with load-line

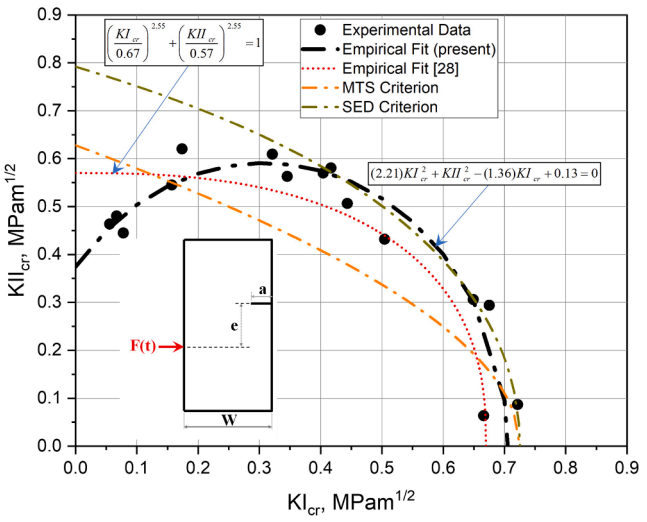

Fig. 10. Mixed-mode fracture envelopes for soda-lime glass.

eccentricity is observed. Using the critical stress intensity factors at crack initiation, a fracture envelope was generated for SLG. The relationship between the effective critical stress intensity factors, $(K_{eff})_{cr}$, and critical mode-mixity, ψ_{cr}, was obtained as a fracture characteristic of the material. The $(K_{eff})_{cr}$ values remain nearly constant until a mode-mixity of ~ 65° and then rapidly decreases until ~ 85°, the maximum mixity achieved in this work. This behavior seems to be analogous to decrease in material strength of borosilicate glass as the imposed shear stress increases, reported in the literature. The kink angles at crack initiation were measured directly from the fractured specimens. The predicted kink angles for MTS and SED criteria were also quantified separately using measured critical stress intensity factors. Reasonably good agreement of measured kink angles with MTS and SED predictions are observed. However, the fracture envelope based on neither of these popular criteria for brittle materials match well with measurements at higher mode-mixities. An empirical quadratic fit of data seems to follow the measured trends well. The resulting critical SIF values of ~ 0.71 MPa$\sqrt{m}$ and ~ 0.37 MPa$\sqrt{m}$, respectively, for mode-I and -II states are obtained.

Table 2
Measured kink angles from experiments along with MTS and SED criteria predicted angles based on critical SIF at initiation. (Measurement accuracy is ± 2°).

Eccentricity ratio, e/W	Measured Kink Angle, deg	MTS criterion, α, deg	SED criterion, β, deg
0	5	11	9
0.12	33	39	33
0.24	47	51	44
0.36	52	59	56
0.48	63	65	67
0.60	68	68	72

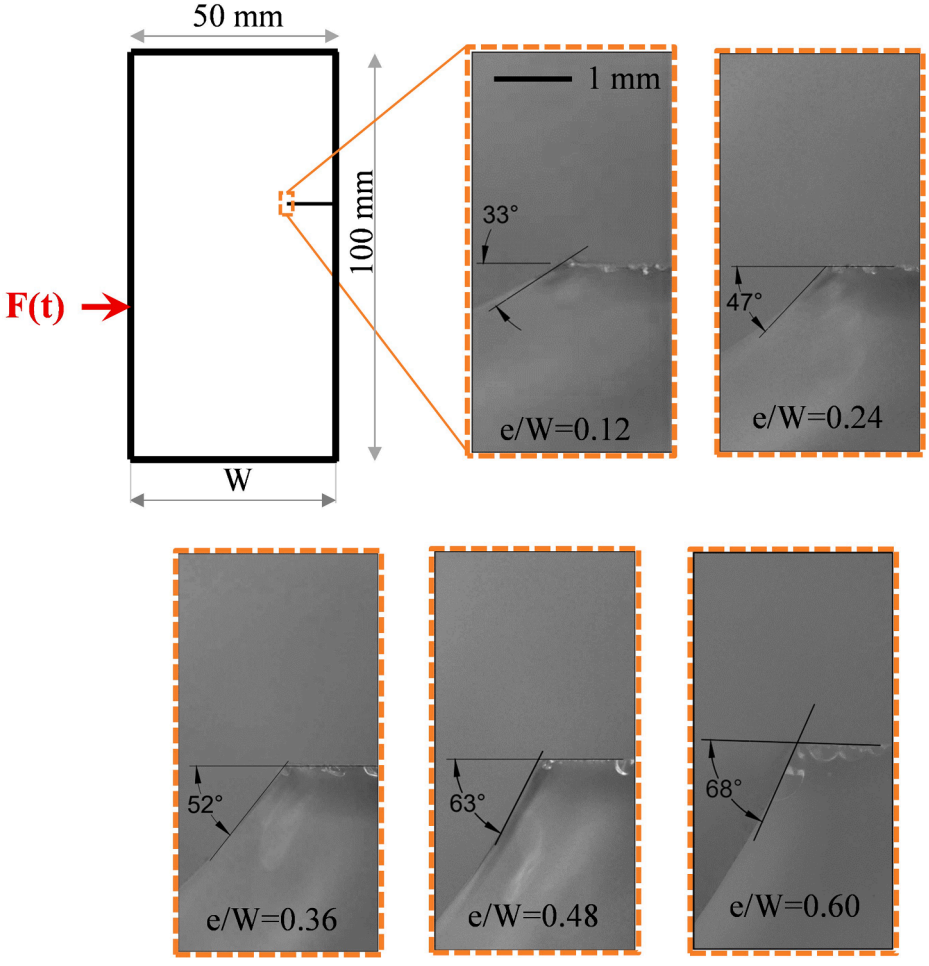

Fig. 11. Measured kink angles obtained from soda-lime glass from different dynamic fracture experiments. Measurement accuracy is ± 2°.

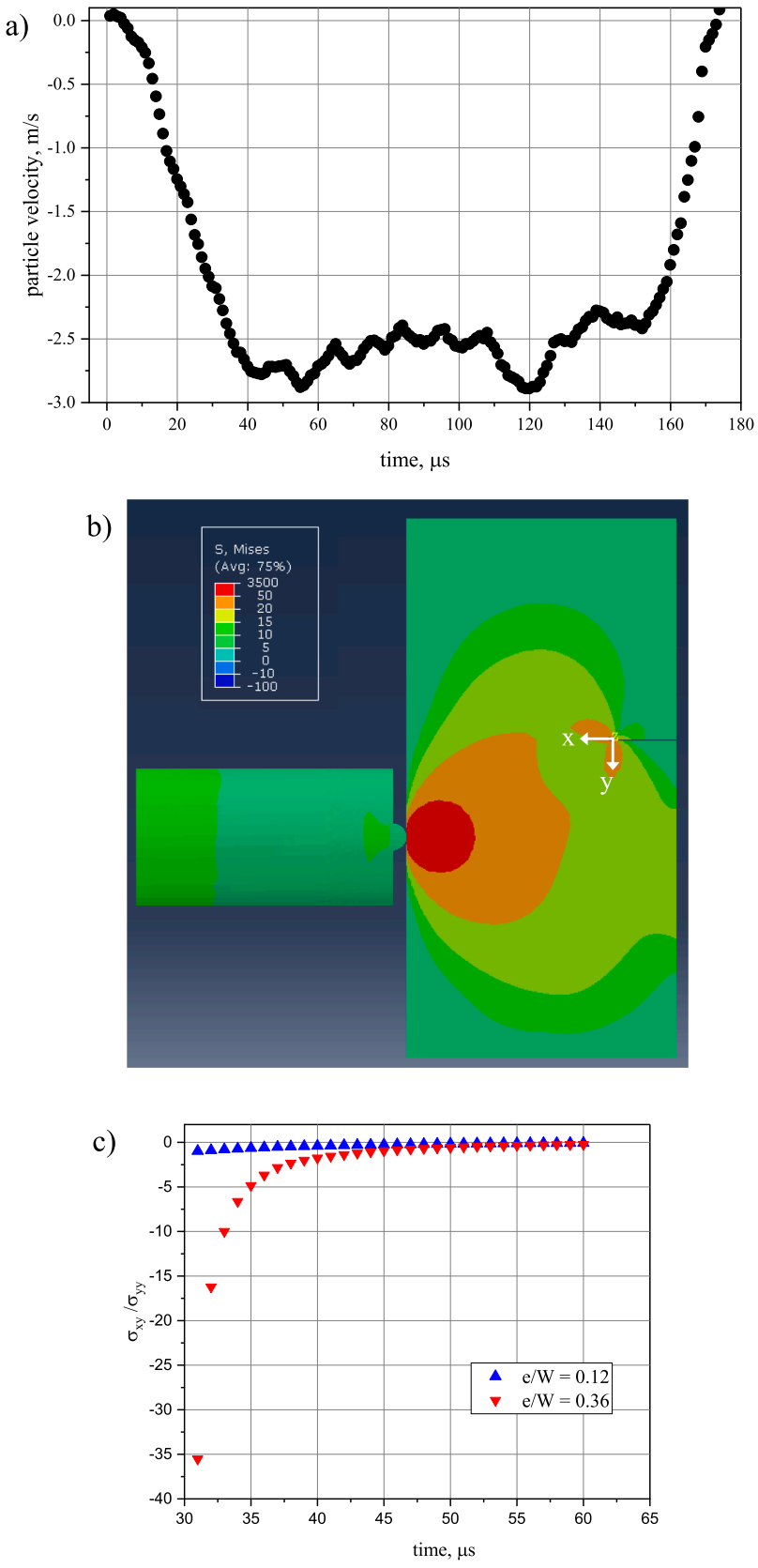

Fig. A1. Numerical simulation for specimen design: a) Particle velocity input to finite element model, b) Instantaneous Von Mises stress distribution in the specimen, c) stress ratio history for eccentricity ratios of, $e/W = 0.12$ and 0.36 cases.

Declaration of Competing Interest

The authors declare that they have no known competing financial interests or personal relationships that could have appeared to influence the work reported in this paper.

Data availability

Data will be made available on request.

Acknowledgements

The authors gratefully acknowledge the support of the U.S. Army Research Office (ARMY-W911NF-22-1-0015) for partially funding this research.

Appendix A

The mixed-mode fracture specimen geometry and loading configurations were conceived by performing explicit elasto-dynamic simulations using Abaqus structural analysis software (Abaqus/CAE 2016). The 3D simulations consisted of a descritized model of the long-bar in contact with the cracked free-free specimen subjected to single point impact using the particle velocity as input for the intended impact velocity of the striker used in the actual experiments. The specimen consisted of 172,000 elements (type C3D10M) and 254,437 nodes and crack tip region was refined to capture the shear and normal stress histories accurately. The details on the impacting bar, element type and nodes are suppressed here for brevity. Fig. A1 shows the particle velocity history (Fig. A1(a)) used in the simulations (for an intended striker velocity of 5.3 m/s) along with an instantaneous von Mises stress field in the specimen (Fig. A1(b)) at a time instant of 47 μs after impact. The history of the ratio of the shear to normal stress ahead of the notch at a location ($r = 1$ mm, $\theta = 0^\circ$) is plotted for two specimen configurations with load-line eccentricity ratios of $e/W = 0.12$ and 0.36 are shown in Fig. A1(c). The histories of stress ratios clearly show that influence of eccentricity on the instantaneous state of stress near the crack tip. For example, if the crack were to initiate hypothetically at a time instant of say 35 μs after impact (Fig. A1(c)), the larger eccentricity specimen would initiate with a higher mode-II component relative to the lower eccentricity specimen configuration. This clearly suggests the feasibility of this geometry to generate a wide range of mode-mixities at crack initiation.

Appendix B. Supplementary data

Supplementary data to this article can be found online at https://doi.org/10.1016/j.tafmec.2023.103791.

References

[1] J.J. Mason, J. Lambros, A.J. Rosakis, The use of a coherent gradient sensor in dynamic mixed-mode fracture mechanics experiments, J. Mech. Phys. Solids 40 (3) (1992) 641–661, https://doi.org/10.1016/0022-5096(92)80007-D.
[2] Z.K. Guo, A.S. Kobayashi, N.M. Hawkins, Dynamic mixed mode fracture of concrete, Int. J. Solids Struct. 32 (17) (1995) 2591–2607, https://doi.org/10.1016/0020-7683(94)00284-4.
[3] M.S. Kirugulige, H.V. Tippur, Mixed-mode dynamic crack growth in functionally graded glass-filled epoxy, Exp. Mech. 46 (2006) 269–281, https://doi.org/10.1007/s11340-006-5863-4.
[4] M. Kirugulige, H.V. Tippur, Mixed-mode dynamic crack growth in a functionally graded particulate composite: experimental measurements and finite element simulations, J. Appl. Mech. 75 (5) (2008), 10.1115/1.2932095.
[5] M.S. Kirugulige, H.V. Tippur, Measurement of fracture parameters for a mixed-mode crack driven by stress waves using image correlation technique and high-speed digital photography, Strain 45 (2) (2009) 108–122, https://doi.org/10.1111/j.1475-1305.2008.00449.x.
[6] A.S. Jain, H.V. Tippur, Mapping static and dynamic crack-tip deformations using reflection-mode digital gradient sensing: applications to Mode-I and mixed-mode fracture, J. Dyn. Behavior Mater. 1 (2015) 315–329, https://doi.org/10.1007/s40870-015-0024-4.
[7] B.M. Sundaram, H.V. Tippur, Dynamic mixed-mode fracture behaviors of PMMA and polycarbonate, Eng. Fract. Mech. 176 (2017) 186–212, https://doi.org/10.1016/j.engfracmech.2017.02.029.
[8] M.J. Braunagel, W.A. Griffith, Microstructural controls on mixed mode dynamic fracture propagation in crystalline and porous granular rocks, J. Geophys. Res.: Solid Earth, 2022. 127(3): p. e2021JB022528.DOI: https://doi.org/10.1029/2021JB022528.
[9] T. Snow, W. Woolley, R.M. Metcalf, J. Rosenberg, C. Acevedo, O.T. Kingstedt, Effect of collagen damage induced by heat treatment on the mixed-mode fracture behavior of bovine cortical bone under elevated loading rates, Int. J. Fract. Mech. 233 (1) (2022) 85–101, https://doi.org/10.1007/s10704-021-00612-0.
[10] M.R.M. Aliha, S.S. Samareh-Mousavi, M.M. Mirsayar, Loading rate effect on mixed mode I/II brittle fracture behavior of PMMA using inclined cracked SBB specimen, Int. J. Solids Struct. 232 (2021), 111177, https://doi.org/10.1016/j.ijsolstr.2021.111177.
[11] R.C. Morales, J. Baek, D. Sharp, A. Aderounmu, H. Wei, J.S. Chen, V. Eliasson, Mode-II Fracture Response of PMMA Under Dynamic Loading Conditions, J. Dynamic Behavior Mater. 8 (1) (2022) 104–121, https://doi.org/10.1007/s40870-021-00320-9.
[12] M.R.M. Aliha, A. Bahmani, Rock fracture toughness study under mixed mode I/III loading, Rock Mech. Rock Eng. 50 (7) (2017) 1739–1751, https://doi.org/10.1007/s00603-017-1201-7.
[13] I. Asareh, Y.C. Yoon, J.H. Song, A numerical method for dynamic fracture using the extended finite element method with non-nodal enrichment parameters, Int. J. Impact Eng 121 (2018) 63–76, https://doi.org/10.1016/j.ijimpeng.2018.06.012.
[14] M. Imachi, S. Tanaka, T.Q. Bui, Mixed-mode dynamic stress intensity factors evaluation using ordinary state-based peridynamics, Theor. Appl. Fract. Mech. 93 (2018) 97–104, https://doi.org/10.1016/j.tafmec.2017.07.008.
[15] Z. Cheng, G. Zhang, Y. Wang, F. Bobaru, A peridynamic model for dynamic fracture in functionally graded materials, Compos. Struct. 133 (2015) 529–546, https://doi.org/10.1016/j.compstruct.2015.07.047.
[16] D. Grégoire, H. Maigre, J. Réthoré, A. Combescure, Dynamic crack propagation under mixed-mode loading–comparison between experiments and X-FEM simulations, Int. J. Solids Struct. 44 (20) (2007) 6517–6534, https://doi.org/10.1016/j.ijsolstr.2007.02.044.
[17] A. Kidane, V.B. Chalivendra, A. Shukla, R. Chona, Mixed-mode dynamic crack propagation in graded materials under thermo-mechanical loading, Eng. Fract. Mech. 77 (14) (2010) 2864–2880, https://doi.org/10.1016/j.engfracmech.2010.07.004.
[18] G. Ruiz, A. Pandolfi, M. Ortiz, Three-dimensional cohesive modeling of dynamic mixed-mode fracture, Int. J. Numer. Meth. Eng. 52 (1–2) (2001) 97–120, https://doi.org/10.1002/nme.273.
[19] S. Dondeti, H.V. Tippur, A Comparative Study of Dynamic Fracture of Soda-Lime Glass Using Photoelasticity, Digital Image Correlation and Digital Gradient Sensing Techniques, Exp. Mech. 60 (2) (2020) 217–233, https://doi.org/10.1007/s11340-019-00549-5.
[20] S. Dondeti, H.V. Tippur, Crack initiation and slow growth in soda-lime glass from a self-healed crack, Theor. Appl. Fract. Mech. 119 (2022), 103341, https://doi.org/10.1016/j.tafmec.2022.103341.
[21] Glass and glass-ceramic. Available from: https://www.makeitfrom.com/material-properties/Soda-Lime-Float-Glass.
[22] C. Periasamy, H.V. Tippur, Full-field digital gradient sensing method for evaluating stress gradients in transparent solids, Appl. Opt. 51 (12) (2012) 2088–2097, https://doi.org/10.1364/AO.51.002088.
[23] S. Dondeti, H.V. Tippur, Cascading Crack Bifurcations in Soda-Lime Glass: Quantification of Fracture Mechanics-Based Precursors Using Digital Gradient Sensing, Int. J. Solids Struct. (2021), 111252, https://doi.org/10.1016/j.ijsolstr.2021.111252.
[24] B.M. Sundaram, H.V. Tippur, Full-field measurement of contact-point and crack-tip deformations in soda-lime glass. Part-I: Quasi-static Loading, Int. J. Appl. Glas. Sci. 9 (1) (2018) 114–122, https://doi.org/10.1111/ijag.12278.
[25] B.M. Sundaram, H.V. Tippur, Dynamic fracture of soda-lime glass: A full-field optical investigation of crack initiation, propagation and branching, J. Mech. Phys. Solids 120 (2018) 132–153, https://doi.org/10.1016/j.jmps.2018.04.010.
[26] E.A. Zimmermann, M.E. Launey, H.D. Barth, R.O. Ritchie, Mixed-mode fracture of human cortical bone, Biomaterials 30 (29) (2009) 5877–5884, https://doi.org/10.1016/j.biomaterials.2009.06.017.
[27] X. Nie, W.W. Chen, X. Sun, D.W. Templeton, Dynamic failure of borosilicate glass under compression/shear loading experiments, J. Am. Ceram. Soc. 90 (8) (2007) 2556–2562, https://doi.org/10.1111/j.1551-2916.2007.01819.x.

[28] S. Tan, X. Yao, S. Long, X. Zhang, S. Zang, Static and dynamic strength of soda-lime glass under combined compression-shear loading, J. Non Cryst. Solids 516 (2019) 14–25, https://doi.org/10.1016/j.jnoncrysol.2019.04.024.
[29] I.L. Lim, I.W. Johnston, S.K. Choi, J.N. Boland, Fracture testing of a soft rock with semi-circular specimens under three-point bending. Part 2—mixed-mode, Int. J. Rock Mech. Mining Sci. Geomech. Abstracts 31 (3) (1994) 199–212, https://doi.org/10.1016/0148-9062(94)90464-2.
[30] M.M. Mirsayar, A. Razmi, F. Berto, Tangential strain-based criteria for mixed-mode I/II fracture toughness of cement concrete, Fatigue Fract. Eng. Mater. Struct. 41 (1) (2018) 129–137, https://doi.org/10.1111/ffe.12665.
[31] M.M. Mirsayar, A. Razmi, M.R.M. Aliha, F. Berto, EMTSN criterion for evaluating mixed mode I/II crack propagation in rock materials, Eng. Fract. Mech. 190 (2018) 186–197, https://doi.org/10.1016/j.engfracmech.2017.12.014.
[32] F. Erdogan, G.C. Sih, On the Crack Extension in Plates Under Plane Loading and Transverse Shear, J. Basic Eng. 85 (4) (1963) 519–525, https://doi.org/10.1115/1.3656897.
[33] C.T. Sun, Z.H. Jin, Chapter 5 - Mixed Mode Fracture, in: C.T. Sun, Z.H. Jin (Eds.), Fracture Mechanics, Academic Press, Boston, 2012, pp. 105–121.